Structural Characterizations of Copper Incorporated Manganese Oxide OMS-2 Material and Its Efficiencies on Toluene Oxidation

SCHOLARONE™
Manuscripts

1 **Structural Characterizations of Copper Incorporated Manganese Oxide OMS-**

2 **2 Material and Its Efficiencies on Toluene Oxidation**

3 C. Kaewbuddee[a,b], P. Chirawatkul[c], K. Kamonsuangkasem[c], N. Chanlek[c] and K. Wantala[a,b,d]*

4

5 [a] *Department of Chemical Engineering, Faculty of Engineering, Khon Kaen University,*

6 *Khon Kaen 40002, Thailand*

7 [b] *Chemical Kinetics and Applied Catalysis Laboratory (CKCL), Faculty of Engineering,*

8 *Khon Kaen University, Khon Kaen 40002, Thailand*

9 [c] *Synchrotron Light Research Institute (Public Organization), 111 University Avenue,*

10 *Muang District, Nakhon Ratchasima, 30000, Thailand*

11 [d] *Research Center for Environmental and Hazardous Substance Management (EHSM),*

12 *Faculty of Engineering, Khon Kaen University, Khon Kaen 40002, Thailand*

13 **Corresponding author: kitirote@kku.ac.th*

14

15 **Detailed contact information**

16 Chatkamol Kaewbuddee

17 Department of Chemical Engineering, Faculty of Engineering, Khon Kaen University,

18 Khon Kaen 40002, Thailand

19 Email: k_chatkamol@kkumail.com

20

21 Prae Chirawatkul

22 Synchrotron Light Research Institute (Public Organization), Nakhon Ratchasima 30000, Thailand

23 Email: prae@slri.or.th

24

25 Krongthong Kamonsuangkasem

26 Synchrotron Light Research Institute (Public Organization), Nakhon Ratchasima 30000, Thailand

27 Email: krongthong@slri.or.th

28

29 Narong Chanlek

30 Synchrotron Light Research Institute (Public Organization), Nakhon Ratchasima 30000, Thailand

31 Email: narong@slri.or.th

32

33 Kitirote Wantala *Corresponding author

34 Department of Chemical Engineering, Faculty of Engineering, Khon Kaen University,

35 Khon Kaen 40002, Thailand

36 Email: kitirote@kku.ac.th

37 Tel.: +66-43-009700 Ext. 45705; Fax: +664 3462 240

1
2
3
4
5
6
7
8
9
10
11
12
13
14
15
16
17
18
19
20
21
22
23
24
25
26
27
28
29
30
31
32
33
34
35
36
37
38
39
40
41
42
43
44
45
46
47
48
49
50
51
52
53
54
55
56
57
58
59
60

38 **Structural Characterizations of Copper Incorporated Manganese Oxide OMS-**

39 **2 Material and Its Efficiencies on Toluene Oxidation**

40 **Abstract**

41 This work aimed to study the excellent properties of the high-valent copper doped into the

42 framework structure of K-OMS-2 catalyst (Cu-K-OMS-2). The physicochemical properties of

43 Cu-K-OMS-2 material were examined using X-ray Diffractometer (XRD), N_2 adsorption-

44 desorption, X-ray photoelectron spectroscopy (XPS), X-ray absorption near edge structure

45 (XANES) and extended X-ray absorption fine structure (EXAFS) techniques. The copper dopant

46 can improve the physicochemical properties of K-OMS-2 catalyst including the specific surface

47 area, O_{ads}/O_{latt} ratio and Cu^{3+}/Cu^{2+} ratio, resulting in enhanced catalytic activity. The Cu^{3+} species

48 were observed in the Cu-K-OMS-2 structure. In addition, the oxidation state of copper on the Cu-

49 K-OMS-2 surface revealed both Cu^{3+} and Cu^{2+} species, which affected toluene removal. The

50 existence of the Cu^{3+}/Cu^{2+} ratio led to enhance toluene removal at low reaction temperature.

51 Moreover, the Cu K-edge EXAFS spectrum demonstrated that the Cu ions existed in the same site

52 as the Mn ions in the K-OMS-2 framework structure. Consequently, we can propose that Cu^{3+}

53 existed in the Cu-K-OMS-2 framework structure by Mn^{3+} substitution in the MnO_6 octahedral site,

54 which influenced the high toluene oxidation at low reaction temperature. In addition, the high-

55 valent copper doped into K-OMS-2 catalyst showed high stability for VOCs oxidation. The

56 activation energy of toluene oxidation over Cu-K-OMS-2 catalyst was computed as shown about

57 91.18 kJ mol^{-1}.

58

59 Keywords: Trivalent copper; Divalent copper; Toluene oxidation; Oxidation state; OMS-2; Cu-K-

60 OMS-2

61

Introduction

62

63 The catalytic oxidation technology with cryptomelane (K-OMS-2) has been widely used for the

64 removal of volatile organic compounds (VOCs) in the gaseous phase (Fu et al., 2017; Hou et al.,

65 2013b; Said et al., 2016; Santos et al., 2011, 2010; Sihaib et al., 2017; Wang and Li, 2010). The

66 high catalytic performance of K-OMS-2 is related to its unique structural properties such as open

67 tunnel structure, mixed-valent manganese oxide, mobile and lattice oxygen species, high specific

68 surface area, hydrophobicity and easy release of lattice oxygen (DeGuzman et al., 1994; Hou et

69 al., 2018, 2013a; Luo et al., 2008, 2000; Shen et al., 2011; Suib, 2008). The excellent properties

70 correlate with the particle morphology and synthesis route (Schurz et al., 2009). The nest-like K-

71 OMS-2 catalyst, synthesized via the hydrothermal method, exhibits a high catalytic activity due to

72 the high concentration of oxygen species and good mobility of oxygen species (Deng et al., 2014).

73 Hou et al. reported that the presence of Mn^{3+} in the OMS-2 samples could imply oxygen vacancy

74 defects, which affect the catalytic oxidation ability of OMS-2 (Hou et al., 2013a). In addition,

75 rising the oxygen vacancy defect concentrations considerably enhances the lattice oxygen

76 reactivity and increasing VOCs removal, for example, benzene (Hou et al., 2013a; Yodsa-nga et

77 al., 2015), toluene (Fu et al., 2017), carbon monoxide (Chen et al., 2008), peroxymonosulfate

78 (Fang et al., 2017) and ozone (Jia et al., 2016; Wang et al., 2015). Moreover, the K-OMS-2 catalyst

79 with high O_{ads}/O_{latt} mole ratio influences the enhancement of the VOCs' oxidation (Jia et al., 2016;

80 L. Liu et al., 2017; H. Sun et al., 2017). However, the K-OMS-2 material displays complete VOCs

81 oxidation at high reaction temperature (more than 250ºC) (Gandhe et al., 2007; Genuino et al.,

82 2012; Liu et al., 2017; Sun et al., 2011; Sun et al., 2015). Thus, the material's efficiency is

83 necessarily improved owing to the deactivation of K-OMS-2 catalyst at low reaction temperature,

84 whereas complete oxidation at high reaction temperature.

85   To modify K-OMS-2 structural properties and catalytic performance, the K-OMS-2

86   material has been modified by doping with several metal cations into the tunnels and/or the

87   framework. Alkali metals are usually incorporated into the tunnel sites of K-OMS-2, such as Li^+,

88   Na^+, K^+, Rb^+ and Cs^+ (Carabineiro et al., 2016; Liu et al., 2003; Santos et al., 2012, 2009; Wu et

89   al., 2011). These metal ions can replace K^+ or occupy empty sites or replace H_3O^+ in tunnel sites

90   (Santos et al., 2012). Hou et al. reported that the substitution of tunnel K^+ ions leads to an increase

91   in the formation energy of an oxygen vacancy, resulting in decreased oxygen vacancy

92   concentration, as a reason why low catalytic activity occurred (Hou et al., 2014). Depending on

93   the results of our literature review, doping metal ions into the framework structure might enhance

94   the K-OMS-2 performance. Transition metal ions have been used to dope the framework of K-

95   OMS-2, for example, W^{6+}, Mo^{6+}, V^{5+}, Cr^{4+}, Fe^{3+}, Ru^{3+}, Cu^{2+}, Zn^{2+}, Co^{2+}, Pt^{2+}, Pd^{2+}, Ni^{2+} and Ag^+

96   (Adjimi et al., 2017; Calvert et al., 2008; Ching et al., 2016; Hernández et al., 2012, 2010;

97   Jothiramalingam et al., 2006a; Li et al., 2015; Ma et al., 2017; Özacar et al., 2013; Roozeboom et

98   al., 1981; Shaikjee and Coville, 2011; Sun et al., 2013). Among those dopants, copper ion shows

99   as a suitable metal ion for modification of K-OMS-2, since it can be prepared by a simple synthesis

100   and it gives an effective oxidation catalyst. The presence of copper ions in K-OMS-2 catalyst

101   improves the catalytic properties associated with the average oxidation state, specific surface area,

102   reducibility, mixed-valent manganese species, oxygen mobility, defect-oxide species and stability

103   (Chen et al., 2001; Hernández et al., 2012, 2010; Liu et al., 2010; Yang et al., 2014; Yun et al.,

104   2017). In addition, the electronegativity property of metal dopants plays an important role in K-

105   OMS-2 performance. Sun et al. (Sun et al., 2013) reported that the metal electronegativity (Cu >

106   Co > Fe > Cr) is related to the order of catalytic activity using transition-metal-ion doped OMS-2

107   catalysts. Because the higher electronegativity leads to a weakness of the Mn–O bond in the Mn–

108　O–M bridge, and the greater mobility and reactivity of the active oxygen species. According to the

109　theory, there are many oxidation states of copper, including Cu^+, Cu^{2+}, Cu^{3+} and Cu^{4+}, which show

110　different electronegativities (Li and Xue, 2006). The copper ions with an increase in the oxidation

111　state possibly increase the electronegativity as follows: $Cu^+ < Cu^{2+} < Cu^{3+} < Cu^{4+}$. Consequently,

112　Cu^{4+} could show the highest efficiency and higher than Cu^{3+}, Cu^{2+} and Cu^+. Commonly, the Cu^{2+}

113　was successfully doped on K-OMS-2 material by several methods, such as reflux (Liu et al., 2010),

114　ball milling (Hernandez et al., 2012), incipient wetness impregnation (Davo-Quinonero et al.,

115　2016), solid-state (Hernandez et al., 2012) and hydrothermal methods (Jothiramalingam et al.,

116　2006b; Ramstad and Mikkelsen, 2004). The Cu^{2+} ions were incorporated in the tunnel structure of

117　K-OMS-2 materials (Jothiramalingam et al., 2006b; Yang et al., 2014), which might destroy the

118　framework structure to become a layer structure resulted in low catalytic activity for VOCs

119　removal (Yang et al., 2014).

120　　　　Recently, we can dope a trivalent copper (Cu^{3+}) into the K-OMS-2 catalyst through the in

121　situ hydrothermal methods (Kaewbuddee et al., 2019a). The effect of hydrothermal conditions on

122　Cu-K-OMS-2 synthesis including aging temperature, aging time and amount of copper dopant

123　were studied by using the Box-Behnken design (BBD) method. The Cu-K-OMS-2 samples were

124　tested with thermal toluene oxidation. The results indicated that the hydrothermal conditions affect

125　the physical and chemical properties and the performance of the Cu-K-OMS-2 catalyst. In

126　addition, the optimal conditions for the Cu-K-OMS-2 synthesis are determined as 120ºC of aging

127　temperature, 6 h of aging time and 6% mole of Cu on K-OMS-2, which exhibited a complete

128　toluene oxidation at low reaction temperature. According to the review, the incorporation of copper

129　in the K-OMS-2 tunnel structure showed a disadvantage in its performance. Therefore, the location

130　of copper ions in K-OMS-2 structure affects the thermal oxidation of VOCs. Continuously, the

131   Cu-K-OMS-2 catalyst, prepared by in situ hydrothermal method at optimal condition, was used to

132   study the excellent properties on toluene oxidation. The local structure of copper in K-OMS-2

133   material was investigated. The stability of Cu-K-OMS-2 catalyst was considered as well.

134   Moreover, the kinetic parameters of toluene oxidation by using Cu-K-OMS-2 were examined. The

135   physicochemical properties of Cu-K-OMS-2 were explained using X-ray diffractometer (XRD),

136   N_2 adsorption-desorption calculated the specific surface area by Brunauer–Emmett–Teller (BET),

137   X-ray photoelectron spectroscopy (XPS), X-ray absorption near edge structure (XANES) and

138   extended X-ray absorption fine structure (EXAFS) techniques.

139

140   **Materials and methods**

141   *Chemicals*

142   All the chemicals used for this study are of analytical grade. Manganese(II) acetate

143   tetrahydrate ($Mn(CH_3COO)_2 \cdot 4H_2O$) with greater than 99% purity, potassium permanganate

144   ($KMnO_4$) with 99% purity and glacial acetic acid (CH_3COOH) were purchased from ACROS

145   Organics, UNIVAR and QRёC, respectively, and 1000-ppm Cu AAS standard solution from

146   Applichem.

147

148   *In situ copper-doped K-OMS-2 (Cu-K-OMS-2) synthesis*

149   Cu-K-OMS-2 was synthesized through a hydrothermal method which was applied following

150   Kaewbuddee et al. research (Kaewbuddee et al., 2019a). First, the mole ratio of 0.75

151    $KMnO_4/Mn(CH_3COO)_2$ was used to prepare the catalyst. The $KMnO_4$ and $Mn(CH_3COO)_2$ were

152   dissolved separately in 40 mL deionized water under continuous stirring until becoming a perfectly

153   mixed solution. Second, the $KMnO_4$ solution was dropped slowly into the $Mn(CH_3COO)_2$ solution

154   and then the 6% mole of copper standard solution was added to the mixture under continuous

155   stirring. Third, the pH of the mixed solution was adjusted to an acidic condition (pH lower than

156   3.5) by concentrated glacial acetic acid and stirred continuously for an hour. After that, the final

157   solution was transferred into an autoclave for the hydrothermal process at 120ºC for 6 h. Finally,

158   the obtained black slurry was filtered and washed with deionized water until the filtrate was pH

159   neutral. The obtained catalyst was dried overnight at 100ºC. The K-OMS-2 was prepared by the

160   same technique with Cu-K-OMS-2 following the optimal condition reported by Yodsa-nga et al.

161   (Yodsa-nga et al., 2015).

162

163   *Catalyst characterization*

164   The crystalline phase of the samples was analyzed by XRD (PANalytical, EMPYREAN

165   (Netherlands)) using Cu Kα radiation with wavelength $\lambda = 0.1514$ nm at 40 mA and 45 kV and

166   Bruker D8 Advance using Cu Kα with wavelength $\lambda = 0.1514$ nm at 30 mA and 40 kV. The specific

167   surface area was analyzed using a N_2 adsorption–desorption analyzer (ASAP2460, Micromeritics,

168   USA) and calculated using the BET equation. The oxidation states of manganese, copper and

169   oxygen were determined by XPS and XANES techniques (BL5.3 and BL1.1W, respectively),

170   Synchrotron Light Research Institute (Public Organization), Thailand. The neighboring atoms and

171   absorber-neighbor distances were analyzed via the EXAFS technique (BL1.1W). The stand-alone

172   XPS with a Kratos AXIS Ultra model was operated using monochromatic Al Kα $h\nu = 1486.71$

173   eV, 5 mA and 15 kV as an X-ray source.

174

175   *Catalytic thermal oxidation of toluene*

176   The catalytic activities of Cu-K-OMS-2 and K-OMS-2 samples were tested in toluene degradation

177   via packed bed reactor (PBR), the same apparatus as in our previous work, where 0.01 g of Cu-K-

178   OMS-2 or K-OMS-2 catalysts were placed in the center of the PBR. Toluene was maintained at –

179   3ºC, using the cold bath as an evaporator. Approximately 7,550 ppmV of toluene concentration,

180   calculated following Doucet et al. (Doucet et al., 2006), was studied. The gaseous toluene

181   oxidation was investigated with reaction temperature in the range of 140–300ºC and the weight

182   hourly space velocity (WHSV) was used at 3.41 h^{-1} under atmospheric pressure. Then, the kinetic

183   parameters were investigated by varying the amount of Cu-K-OMS-2 catalyst between 0.005-0.02

184   g. Additionally, to study the catalytic stability and the deactivation of Cu-K-OMS-2 catalyst, the

185   toluene concentration was set up to 13,500 ppmV (about 2 times), then passed through 0.15 g of

186   catalyst in the PBR at 200ºC of reaction temperature. After the toluene oxidation, the spent

187   catalysts were studied the characteristic, such as the phase structure or the binding energy of XPS

188   compared with the fresh catalyst. The toluene concentration in the fluid was measured using gas

189   chromatography with a thermal conductivity detector using Gaskuropack 54 as a column (GC-

190   TCD, Shimadzu, 8A series, Japan) which was investigated at least three times for each reaction-

191   temperature testing. The percentage removal of toluene (Y) was calculated using Equation (1).

$$Y = \frac{C_0 - C_f}{C_0} \times 100\%,\tag{1}$$

193   where C_0 and C_f are toluene concentrations before and after reaction in the PBR, respectively.

194

Results and discussion

Characterizations

197   The XRD patterns of the prepared catalysts are presented in Figure 1. According to the previous

198   work, Yodsa-nga et al. found the optimum conditions of K-OMS-2 synthesis for VOCs removal

199   at 75ºC of aging temperature for 21 h of aging time (Yodsa-nga et al., 2015). Therefore, the K-

200   OMS-2 sample as an undoped reference catalyst, synthesized by following Yodsa-nga et al.

201   (Yodsa-nga et al., 2015), presented characteristic peaks at 2θ values of 12.73, 18.21, 28.76, 37.51,

202   41.89, 50.08, 60.17, 65.32 and 70º which correspond to the cryptomelane type (JCPDS 29-1020,

203   KMn_8O_{16}) (Iyer et al., 2010; Kumar et al., 2009; Sithambaram et al., 2009). According to our

204   results, the XRD patterns of Cu-K-OMS-2 catalyst clearly showed the cryptomelane (K-OMS-2)

205   phase structure. Moreover, no additional peaks were observed, indicating that the Cu-K-OMS-2

206   materials were a pure phase of K-OMS-2 and the copper oxide phase was not observed. The results

207   implied that copper ions were well dispersed or incorporated into the K-OMS-2 structure and the

208   copper amounts did not damage the Cu-K-OMS-2 crystalline phase as well.

209

210   [Figure 1 near here]

211

212   [Table 1 near here]

213

214   The specific surface areas of prepared samples were measured using a N_2 adsorption–

215   desorption analyzer and calculated by the BET equation, as shown in Table 1. The results found

216   that the copper dopant influenced the specific surface area of the K-OMS-2 catalyst. Obviously,

217   the specific surface areas of Cu-K-OMS-2 samples are higher than undoped K-OMS-2 prepared

218   at optimal condition reported by Yodsa-nga et al. (Yodsa-nga et al., 2015). Therefore, the K-OMS-

219   2 materials were doped with the copper dopant, in which the specific surface area was higher than

220   without doping. The higher specific surface areas of Cu-K-OMS-2 materials could have promoted

221   the catalytic activity. Likewise, Kaewbuddee et al. research, they reported that the K-OMS-2

222 catalyst with a high specific surface area showed the highest toluene removal (Kaewbuddee et al.,

223 2019b).

224

225 [Figure 2 near here]

226

227   The copper and manganese species in K-OMS-2 material were investigated by the XANES

228 technique, as presented in Figure 2. The oxidation state of manganese in K-OMS-2 structure was

229 analyzed using the XANES technique with Mn K-edge energy, as shown in Figure 2(a). The Mn

230 K-edge features of manganese standards and prepared Cu-K-OMS-2 materials were explored. The

231 pre-edge features of Cu-K-OMS-2 material and MnO_2 standard were quite the same shape. But,

232 the Cu-K-OMS-2 presented lower intensity of pre-edge than the MnO_2 standard. However, the

233 shoulder peak of Cu-K-OMS-2 materials displayed features similar to the Mn_2O_3 standard. In

234 addition, the Mn K-edge absorption energy (E_0) of Cu-K-OMS-2 materials was determined at

235 ~6,551 eV, which was higher than E_0 of the Mn_2O_3 standard (6,548 eV), but lower than E_0 of the

236 MnO_2 (6,552) standard. These results indicated that the oxidation states of manganese in Cu-K-

237 OMS-2 structure were the mixed-valence states of Mn_2O_3 (3+) and MnO_2 (4+). The Mn^{3+}/Mn^{4+}

238 ratios of Cu-K-OMS-2 and K-OMS-2 samples were estimated by linear combination fitting (LCF)

239 of XANES spectra with MnO_2 and Mn_2O_3 reference materials using Athena software. The LCF

240 results presented that the Mn^{3+}/Mn^{4+} ratio of the Cu-K-OMS-2 sample (0.08) was slightly lower

241 than the K-OMS-2 sample (0.10), as shown in Table 1. This phenomenon might be caused by the

242 replacing of Cu ions in Cu-K-OMS-2 structure. According to Wu et al. work, they found that the

243 amounts of Mn ions in Co-K-OMS-2 and Cu-K-OMS-2 were lower than in the K-OMS-2 material,

244 which indicated that the Mn ions were replaced by Co or Cu ions in the framework of K-OMS-2

245   structure (Wu et al., 2018). The oxidation states of copper in the K-OMS-2 structure were

246   confirmed by the XANES spectra with Cu K-edge energy. The XANES features of copper

247   standards are shown in Figure 2(b). There obviously showed different position edges and shapes.

248   The pre-edge energy of Cu_2O and CuO appeared at 8,977.31 and 8,978.64 eV, respectively,

249   corresponding to the literature (Adak et al., 2017; Munoz-Rojas et al., 2007). To visibly compare

250   the position edges and shapes, copper standards were plotted along with Cu-K-OMS-2 materials,

251   as shown in Figure 2(b). According to our results, the pre-edge energy of Cu-K-OMS-2 catalyst

252   was shifted to 8,980.54 eV, which is correlated with the pre-edge energy of Cu^{3+} species

253   (Chandarak et al., 2011; Munoz-Rojas et al., 2007; Sinha et al., 2015; Tomson et al., 2015). The

254   pre-edge energy of Cu-K-OMS-2 material is higher than the Cu_2O and CuO standards. The results

255   showed that the XANES feature of Cu-K-OMS-2 sample does not match with Cu_2O and CuO

256   standards. The Cu-K-OMS-2 material does not present the shoulder peak, unlike with Cu_2O and

257   CuO standards. In addition, the white line peak of the prepared sample is more intense than both

258   standards, this phenomenon relates to the oxidation state (Gomes et al., 2013). The greater the peak

259   intensity, the wider the white line of the copper absorption edge, demonstrating the higher

260   oxidation state (Chen et al., 2006; Tsai et al., 2004). Therefore, the copper species in K-OMS-2

261   structure was not Cu^+ and Cu^{2+} species, it should be higher than Cu^{2+} species. Likewise, Elias et

262   al. found that the edge position for $Cu_{0.1}Ce_{0.9}O_{2-x}$ sample is higher than CuO standard about 3.2

263   eV, which indicates a formal valence higher than 2+ (a mixture of 2+ and 3+). Then, they

264   confirmed that the weak pre-edge feature of $Cu_{0.1}Ce_{0.9}O_{2-x}$ sample specifies the Cu^{3+} type (Elias et

265   al., 2014). Moreover, Deng et al. reported that the $NaCuO_2$ K-edge shifts by ~2.2 eV, relative to

266   CuO standard. The shift in edge energy demonstrates an increase in the average valence of copper,

267   which can be indicated to the formation of Cu^{3+} (Deng et al., 2016). According to these results, we

268   can propose that the pre-edge position (8,980.54 eV) and the unique XANES features of Cu-K-

269   OMS-2 materials indicated the trivalent copper (Cu^{3+}).

270   [Figure 3 near here]

271

272   Figure 3(a) shows the XPS results. The Cu-K-OMS-2 materials were analyzed for surface

273   oxidation using the XPS technique with Cu 2p spectra with binding energy at 925–970 eV. The

274   Cu 2p XPS spectra can be used to confirm the oxidation state of copper on the Cu-K-OMS-2

275   surface. Normally, the Cu 2p energy level of copper is composed of main characteristic doublet

276   peaks corresponding to Cu $2p_{3/2}$ and Cu $2p_{1/2}$ peaks along with the shake-up satellite structures at

277   ~8 eV and ~10 eV binding energies higher than the main Cu 2p peak. The binding energies at ~931

278   eV and ~951 eV corresponding to Cu $2p_{3/2}$ and Cu $2p_{1/2}$ peaks, respectively, indicate the Cu^+

279   species. In addition, the Cu^{2+} species appear at ~933 eV and ~953 eV, associated with Cu $2p_{3/2}$ and

280   Cu $2p_{1/2}$ energy levels, respectively (Akgul et al., 2014; Kataoka et al., 2011; H. Liu et al., 2017;

281   Natarajan et al., 2018; Rebhan et al., 2015; Sharma et al., 2018). Generally, the XPS spectra of

282   Cu^{3+} oxides are composed of the main peak and satellite feature at $2p3d^{10}L^2$ (~934 eV) and $2p3d^9L$

283   final state (~945 eV), respectively (Kataoka et al., 2011). According to our results (Figure 3(a)),

284   the Cu 2p energy level displayed that the Cu $2p_{3/2}$ spectra overlap with the Cu $2p_{1/2}$ peak position.

285   Remarkably, the Cu $2p_{3/2}$ spectra of Cu-K-OMS-2 materials consisted of two main peaks at 933

286   eV and 936 eV, and a satellite peak located at around 945–946 eV. Clearly, the binding energy of

287   Cu $2p_{3/2}$ spectra were deconvoluted with two components corresponding to the Cu^{2+} and Cu^{3+} at

288   933 eV and 936 eV, respectively. Similarly, Kim et al. found the mixed states of Cu^{2+} and Cu^{3+} in

289   Cu-substituted LaSrMnO samples (Kim et al., 2008). However, we could not propose that the

290   satellite peak of Cu $2p_{3/2}$ spectra refer to the Cu^{3+} state because the background of Cu 2p spectra

291   overlap with Mn LMM (945 eV) region (Chen et al., 2018). Therefore, the Cu^{3+}/Cu^{2+} ratio was

292   computed by based on the fitting results of Cu $2p_{3/2}$ spectra, as shown in Table 1. Consequently,

293   we can suggest that the mixed-valence of Cu^{2+} and Cu^{3+} species existed on the Cu-K-OMS-2

294   surface.

295   The Mn 2p spectra of Cu-K-OMS-2 samples were fitted, as shown in Figure 3(b). The Mn

296   2p energy level of manganese consisted of two characteristic doublet peaks corresponding to Mn

297    $2p_{3/2}$ and Mn $2p_{1/2}$ energy. The doublet peaks of Mn 2p spectra at binding energies ~642 eV and

298   ~654 eV were assigned to Mn^{3+} species; besides, the binding energies at ~644 eV and ~656 eV

299   were assigned to Mn^{4+} species (Biesinger et al., 2011; McManus et al., 2016; F. Pan et al., 2016;

300   Wu et al., 2018, 2017). Therefore, the manganese species on the Cu-K-OMS-2 surface were

301   mixed-valent Mn^{3+} and Mn^{4+} species.

302   The kinds of oxygen species were fitted, as displayed in Figure 3(c). The O 1s spectra of

303   Cu-K-OMS-2 samples were composed of three characteristic peaks corresponding to lattice

304   oxygen (O_{latt}), surface adsorbed oxygen (O_{ads}) and adsorbed molecular water species (O_{wat}). The

305   binding energy peak, located at ~530 eV, was identified to O_{latt} (O_2^{2-}), which is an oxygen species

306   bonded to metal cations in a coordinately saturated environment (Genuino et al., 2013; R. Pan et

307   al., 2016; L. Sun et al., 2011). The binding energy peak at ~531 eV was associated with O_{ads} (O_2^-

308   , O^-), OH^- groups on the surface and oxygen vacancies, which is an oxygen species bonded to

309   metal cations in a coordinately unsaturated environment (Genuino et al., 2013; R. Pan et al., 2016;

310   L. Sun et al., 2011). The binding energy peak, located at ~533 eV, was ascribed to adsorbed

311   molecular water (Genuino et al., 2013; R. Pan et al., 2016; L. Sun et al., 2011). Moreover, the

312   O_{ads}/O_{latt} ratio was estimated from the XPS spectra fitting, as shown in Table 1. The O_{ads}/O_{latt} ratio

313 of Cu-K-OMS-2 catalyst (0.62) was higher than the K-OMS-2 material. Therefore, the copper

314 doped on K-OMS-2 can enhance the O_{ads}/O_{latt} ratio, which promoted the catalytic activity.

315

316   [Figure 4 near here]

317

318   To identify the local atomic environment and demonstrate the substitution of Cu ion in K-

319 OMS-2 material, EXAFS analysis of Cu-K-OMS-2 catalyst with the Mn K-edge and Cu K-edge

320 were performed. The analysis assumed that the Mn ions resided in the corner-sharing octahedral

321 units of the cryptomelane Q structure using the Inorganic Crystal Structure Database (ICSD) 59159

322 as a cryptomelane structural model (Demchenko et al., 2009; Stelmachowski et al., 2018). The

323 cryptomelane model consisted of the first neighboring octahedral O ions, the other neighboring O

324 and Mn ions using the interatomic distance up to 3.5 Å from the central Mn ion. Figure 4(a) shows

325 the EXAFS refinement of the $|\chi(R)|$ (Fourier transform of $\chi(k)$) for the Mn ions in the K-OMS-2

326 structure. The spectrum was a good fit with the R-factor of 1.6% indicated that the cryptomelane

327 Q structure model represented a good model (R-factor < 2%) for the K-OMS-2 structure. In

328 addition, the refinement of the Cu K-edge corresponding with the cryptomelane model, the Mn

329 ion was replaced by Cu ion, as shown in Figure 4(b). The Cu K-edge EXAFS spectrum displayed

330 a good fit with the data (R-factor = 0.1%), demonstrating that the Cu ions existed in the same site

331 as the Mn ions. Moreover, the Cu ions substituted the Mn ions, in which they were doped into the

332 K-OMS-2 framework structure. Likewise, Shen et al. reported that the Fe presented as Fe^{3+} in an

333 octahedral environment similar to Mn in the MnO_6 of K-OMS-2 (Shen et al., 2011). In addition,

334 the structural disorder of all correlations was signified using the EXAFS Debye–Waller factors

335 (σ^2). The refined interatomic distances and σ^2 factors are summarized in Table 2. According to the

336 Cu-substituted fitting, the interatomic distances and σ^2 of the first O and Cu/Mn coordination were

337 slightly higher than the conventional MnO_6 site owing to a local distortion of the K-OMS-2

338 framework structure when Mn ion was replaced by Cu ion. In addition to the XANES, XPS and

339 EXAFS results, we can propose that the Cu ions were doped into the K-OMS-2 framework

340 structure, in which Cu^{3+} species existed predominantly by replacing Mn ions in the octahedral site,

341 as shown in Figure 5.

342

343 [Table 2 near here]

344

345 [Figure 5 near here]

346

347 According to King'ondu et al. (King'ondu et al., 2011), the dopant can be embedded into

348 the octahedral framework by the substitution of MnO_6 units of K-OMS-2, then cations must allow

349 six-coordination and have a crystal radius almost the same size as that of Mn^{3+} (72 pm), Mn^{4+} (67

350 pm). Moreover, the MnO_6 units of K-OMS-2 can be substituted by CuO_6 units, thus a crystal radius

351 of copper in six-coordination must be almost the same size as Mn^{3+} or Mn^{4+}. The crystal radii of

352 Cu^{2+} and Cu^{3+} in six-coordination are 87 and 68 pm, respectively. The Cu ion in this work

353 represented Cu^{3+} species in the K-OMS-2 structure, whereas Yang et al. (Yang et al., 2014)

354 reported that CuO/Cu^{2+} incorporated into the K-OMS-2 framework. Moreover, Elias et al. reported

355 that the Cu-O bond distance was found to be 1.93 Å (similarly with this work), which indicated a

356 contribution of Cu^{3+}(Elias et al., 2014). According to the literature, the MnO_6 units were possibly

357 substituted by Cu^{3+} more than Cu^{2+} to form CuO_6 units because of the crystal radius size, the bond

358 distance and the oxidation state. Therefore, to replace Mn ions in the octahedral site by copper, the

359   oxidation state of copper should be 3+. Then, we can suggest that the MnO_6 units of Cu-K-OMS-

360   2 catalyst in this work were substituted by Cu^{3+} during the formation process of the octahedral site.

361   *Catalytic performance and stability study*

362

363   [Figure 6 near here]

364

365   The catalytic performances of Cu-K-OMS-2 and undoped K-OMS-2 samples were investigated

366   by toluene oxidation in a PBR under the same condition, as presented in Figure 6. These results

367   showed that the Cu-K-OMS-2 catalysts exhibited a higher toluene removal than the undoped K-

368   OMS-2 catalyst at 180ºC of reaction temperature. Additionally, complete oxidation took place at

369   a reaction temperature of 190ºC and 200ºC for Cu-K-OMS-2 and K-OMS-2 catalysts, respectively.

370   The pure phase structure of Cu-K-OMS-2 with high specific surface area and O_{ads}/O_{latt} ratio led to

371   show a high toluene removal. The high specific surface area correlated with high O_{ads}/O_{latt} ratio

372   resulted in high toluene removal, corresponding to Kaewbuddee et al. result (Kaewbuddee et al.,

373   2019b). Moreover, the Cu^{3+} species in Cu-K-OMS-2 framework structure could enhance the

374   toluene removal due to the high electronegativity of Cu^{3+} species. The higher electronegativity

375   leads to a weakness of the Mn–O bond in the Mn–O–M bridge, and the great mobility and

376   reactivity of the active oxygen species resulted in high toluene removal. In addition, Kaewbuddee

377   et al. confirmed that the high amount of copper dopant led to the enhancement of toluene removal.

378   The Cu^{3+}/Cu^{2+} ratio on Cu-K-OMS-2 catalyst increased with the rise in copper dopant, which

379   promoted the toluene removal (Kaewbuddee et al., 2019a). Therefore, the Cu-K-OMS-2 catalysts

380   in this work exhibited a low complete-reaction temperature of toluene oxidation compared with

381   the manganese oxide-based catalyst of other recent researches (Genuino et al., 2012;

382 Tarjomannejad et al., 2016). According to these results, copper doped into the K-OMS-2

383 framework structure can enhance the catalytic performance at a low reaction temperature. The

384 scale-up of the experiment was set to study the catalytic stability and deactivation of the Cu-K-

385 OMS-2 catalyst for toluene oxidation via PBR with 0.15 g of catalyst. The toluene, about 13,500

386 ppmV, was passed through the PBR at a complete reaction temperature of 200ºC for 8 h reaction

387 time. The physicochemical properties of fresh and used catalyst were characterized by XRD and

388 XPS techniques. Figure 1 confirms that the crystalline phase of used Cu-K-OMS-2 was not

389 destroyed after the reaction finished. In addition, the binding energy of Cu, Mn and O elements of

390 used Cu-K-OMS-2 was not shifted compared with fresh Cu-K-OMS-2 catalyst, as shown in Figure

391 3. Therefore, the copper-doped K-OMS-2 catalyst presented a high stability for toluene oxidation

392 at a reaction temperature of 200ºC.

393

394 ***Kinetic study***

395

396   [Figure 7 near here]

397

398 The kinetic parameters of toluene oxidation by using Cu-K-OMS-2 catalyst were studied under

399 the reaction temperature in the range of 130–150ºC with the WHSV at 3.41 h^{-1} and 7,550 ppmV

400 of initial toluene concentration. The initial reaction rates of toluene oxidation were computed by

401 using the correlation of toluene conversion and space time at different reaction temperatures. Then,

402 the relationships between the initial reaction rate of toluene oxidation versus reaction temperature

403 and the natural log of initial reaction rate of toluene oxidation versus inverse reaction temperature

404 were presented in Figure 7(a) and 7(b), respectively. The toluene reaction rate increases with

405 increasing in the reaction temperature. The activation energy (E_a) of toluene oxidation was

406 determined by the combination of the power law models (Equation (2)) and the Arrhenius equation

407 (Equation (3)), following the deep toluene oxidation reaction with oxygen. Based on our

408 experiment, the initial toluene and O_2 are constant concentrations. Likewise, pressure and inlet

409 volumetric flow rate are constant as well.

410

411 The gas-phase reaction rate of toluene is shown in Equation (2).

412
$$-r_0 = k_A P_{toluene,0}^{\propto} P_{oxygen,0}^{\beta} \tag{2}$$

413 Where, $-r_0$ is the initial reaction rate of toluene, k_A is a reaction rate constant, $P_{toluene,0}$ and $P_{oxygen,0}$

414 are initial concentration of toluene and oxygen, respectively.

415 The Arrhenius equation is displayed in Equation (3).

416
$$k_A(T) = Ae^{-E_a/RT} \tag{3}$$

417 Here, A is pre-exponential factor, E_a is the activation energy, R is gas constant and T is absolute

418 temperature (K). Then, combined equation between the power law models and the Arrhenius

419 equation is presented in Equation (4).

420
$$-r_0 = Ae^{-E_a/RT} P_{toluene,0}^{\propto} P_{oxygen,0}^{\beta} \tag{4}$$

421 Give;
$$A' = AP_{toluene,0}^{\propto} P_{oxygen,0}^{\beta} \tag{5}$$

422
$$-r_0 = A'e^{-E_a/RT} \tag{6}$$

423 Where; A' is the constant values as shown in Equation (5). Then, A' substituted to Equation (6) and

424 then this equation is taken to the natural logarithm. The final equation is revealed in Equation (7)

425 to compute the activation energy (E_a).

426
$$\ln r_0 = -\frac{E_a}{RT} - \ln A' \tag{7}$$

427

428   In order to estimate E_a, the natural logs of the initial reaction rate of toluene oxidation and

429    $\ln(r_0)$ were plotted along with the inverse reaction temperature, as presented in Figure 7(b).

430   According to the linear relationship between $\ln(r_0)$ and $1/T$, the activation energy of the toluene

431   oxidation with Cu-K-OMS-2 catalyst was determined to be 91.18 kJ mol^{-1}. The E_a value of this

432   work is lower than the activation energy of the deep toluene oxidation with oxygen system by

433   using platinum on alumina catalyst, which has been reported to be 106 kJ mol^{-1} (Ordonez et al.,

434   2002). In addition, it is significantly lower than the activation energies of total oxidation of toluene

435   with oxygen by using palladium and platinum supported on carbon nanofiber as a catalyst, which

436   has been reported to be between 116–161 kJ mol^{-1} (Morales-Torres et al., 2009). Although the

437   inlet concentration of toluene was higher than other researches, the Cu-K-OMS-2 catalyst in this

438   work presented the highest toluene removal at the low reaction temperature, according to Table 3.

439   Hence, we can propose that the Cu-K-OMS-2 catalyst in this work can enhance the toluene

440   oxidation at low reaction temperature, which exposed a high toluene removal compared with other

441   researches.

442

443   [Table 3 near here]

444

445   **Conclusions**

446   High-valent copper was successfully doped into the K-OMS-2 framework structure by the in situ

447   hydrothermal method. The Cu^{3+} species appeared in the K-OMS-2 structure, which was identified

448   using the XANES technique. In addition, the Cu^{3+} species existed in the Cu-K-OMS-2 framework

449   structure by the Mn^{3+} substitution in the MnO_6 octahedral site, which influenced the high toluene

450   oxidation at the low reaction temperature. Moreover, the oxidation state of copper in Cu-K-OMS-2

451   material exhibited both the Cu^{3+} and Cu^{2+} species on the catalyst surface. The copper dopant can

452   improve the physicochemical properties of Cu-K-OMS-2 catalysts, which is associated with the

453   catalytic performance. The Cu-K-OMS-2 materials exhibited higher toluene removal than

454   undoped K-OMS-2 material at low reaction temperature because they showed a pure phase of the

455   Cu-K-OMS-2 structure, high specific surface area and O_{ads}/O_{latt} ratio. Additionally, the low

456   activation energy of the toluene oxidation with Cu-K-OMS-2 catalyst was observed to be 91.18 kJ

457   mol^{-1}, resulted in the enhancement of toluene removal at low reaction temperature. The complete

458   toluene oxidation took place at 190ºC of reaction temperature. Moreover, the Cu-K-OMS-2

459   catalysts showed high stability for toluene oxidation at low reaction temperature.

460

References

Adak, S., Hartl, M., Daemen, L., Fohtung, E., and Nakotte, H. (2017). Study of oxidation states of the transition metals in a series of Prussian blue analogs using x-ray absorption near edge structure (XANES) spectroscopy, *J. Electron Spectrosc. Relat. Phenom.*, **214**, 8–19.

Adjimi, S., Garcia-Vargas, J.M., Diaz, J.A., Retailleau, L., Gil, S., Pera-Titus, M., Guo, Y., and Giroir-Fendler, A. (2017). Highly efficient and stable Ru/K-OMS-2 catalyst for NO oxidation, *Appl. Catal. B Environ.,* **219**, 459–466.

Akgul, F.A., Akgul, G., Yildirim, N., Unalan, H.E., Turan, R. (2014). Influence of thermal annealing on microstructural, morphological, optical properties and surface electronic structure of copper oxide thin films, *Mater. Chem. Phys.*, **147**, 987–995.

Biesinger, M.C., Payne, B.P., Grosvenor, A.P., Lau, L.W.M., Gerson, A.R., and Smart, R.St.C. (2011). Resolving surface chemical states in XPS analysis of first row transition metals, oxides and hydroxides: Cr, Mn, Fe, Co and Ni, *Appl. Surf. Sci.*, **257**, 2717–2730.

Calvert, C., Joesten, R., Ngala, K., Villegas, J., Morey, A., Shen, X., and Suib, S.L. (2008). Synthesis, characterization, and rietveld refinement of tungsten-framework-doped porous manganese oxide (K-OMS-2) material, *Chem. Mater.*, **20**, 6382–6388.

Carabineiro, S.A.C., Santos, V.P., Pereira, M.F.R., Orfao, J.J.M., Figueiredo, J.L. (2016). CO oxidation over gold supported on Cs, Li and Ti-doped cryptomelane materials, *J. Colloid Interface Sci.*, **480**, 17–29.

Chandarak, S., Jutimoosik, J., Pojprapai, S., Srilomsak, S., Rujirawat, S., Yimnirun, R., and Monnor, T. (2011). Synchrotron X-ray absorption study of Cu and Mn doped $BiFeO_3$-$BaTiO_3$ multiferroic ceramics, *Ferroelectrics.*, **422**, 23–29.

492   Chen, C.H., Sarma, L.S., Wang, G.R., Chen, J.M., Shih, S.C., Tang, M.T., Liu, D.G., Lee, J.F.,

493   Chen, J.M., and Hwang, B.J. (2006). Formation of bimetallic Ag-Pd nanoclusters via the

494   reaction between Ag nanoclusters and Pd2+ ions, *J. Phys. Chem. B*, **110**, 10287–10295.

495   Chen, J., Li, J., Li, H., Huang, X., and Shen, W. (2008). Facile synthesis of Ag–OMS-2 nanorods

496   and their catalytic applications in CO oxidation, *Microporous Mesoporous Mater.* **116**,

497   586–592.

498   Chen, S.Y., Tang, W., He, J., Miao, R., Lin, H.J., Song, W., Wang, S., Gao, P.X., and Suib, S.L.

499   (2018). Copper manganese oxide enhanced nanoarray-based monolithic catalysts for

500   hydrocarbon oxidation, *J. Mater. Chem. A*, **6**, 19047–19057.

501   Chen, X., Shen, Y.F., Suib, S.L., and O'Young, C.L. 2001. Catalytic decomposition of 2-propanol

502   over different metal-cation-doped OMS-2 materials, *J. Catal.*, **197**, 292–302.

503   Ching, S., Carmichael, J.R., Eichelberger, L.A., Kriz, D.A., Alley, K.A., and Jackvony, S.E.

504   (2016). Influence of Fe, Cu, V, and Ce doping on morphology and catalytic activity of

505   amorphous manganese oxide hollow spheres, *Polyhedron*, **114**, 205–212.

506   Davo-Quinonero, A., Navlani-Garcia, M., Lozano-Castello, D., and Bueno-Lopez, A. (2016).

507   CuO/cryptomelane catalyst for preferential oxidation of CO in the presence of H$_2$:

508   deactivation and regeneration, *Catal. Sci. Technol.*, **6**, 5684–5692.

509   DeGuzman, R.N., Shen, Y.F., Neth, E.J., Suib, S.L., O'Young, C.L., Levine, S., and Newsam,

510   J.M., 1994. Synthesis and characterization of octahedral molecular sieves (OMS-2) having

511   the hollandite structure, *Chem. Mater.*, **6**, 815–821.

512   Demchenko, I.N., Lawniczak-Jablonska, K., Tyliszczak, T., Birkner, N.R., Stolte, W.C.,

513   Chernyshova, M., and Hemmers, O. (2009). XANES studies of modified and newly

514   synthesized nanostructured manganese oxides, *J. Electron Spectrosc. Relat. Phenom.*, **171**,

515   24–29.

516 Deng, Y., Handoko, A.D., Du, Y., Xi, S., and Yeo, B.S. (2016). In situ raman spectroscopy of

517   copper and copper oxide surfaces during electrochemical oxygen evolution reaction:

518   Identification of CuIII oxides as catalytically active species, *ACS Catal.*, **6**, 2473–2481.

519 Deng, Y.Q., Zhang, T., Au, C.T., Yin, S.F. (2014). Oxidation of p-chlorotoluene to p-

520   chlorobenzaldehyde over manganese-based octahedral molecular sieves of different

521   morphologies, *Catal. Commun.*, **43**, 126–130.

522 Doucet, N., Bocquillon, F., Zahraa, O., and Bouchy, M. (2006). Kinetics of photocatalytic VOCs

523   abatement in a standardized reactor, *Chemosphere*, **65**, 1188–1196.

524 Elias, J.S., Risch, M., Giordano, L., Mansour, A.N., and Shao-Horn, Y. (2014). Structure, bonding,

525   and catalytic activity of monodisperse, transition-metal-substituted CeO_2 nanoparticles, *J.*

526   *Am. Chem. Soc.*, **136**, 17193–17200.

527 Fang, J., Li, J., Gao, L., Jiang, X., Zhang, J., Xu, A., and Li, X. (2017). Synthesis of OMS-

528   2/graphite nanocomposites with enhanced activity for pollutants degradation in the

529   presence of peroxymonosulfate, *J. Colloid Interface Sci.*, **494**, 185–193.

530 Fu, Z., Liu, L., Song, Y., Ye, Q., Cheng, S., Kang, T., and Dai, H. (2017). Catalytic oxidation of

531   carbon monoxide, toluene, and ethyl acetate over the xPd/OMS-2 catalysts: Effect of Pd

532   loading, *Front. Chem. Sci. Eng.*, **11**, 185–196.

533 Gandhe, A.R., Rebello, J.S., Figueiredo, J.L., Fernandes, J.B. (2007). Manganese oxide OMS-2 as

534   an effective catalyst for total oxidation of ethyl acetate, *Appl. Catal. B Environ.*, **72**, 129–

535   135.

536   Genuino, H.C., Dharmarathna, S., Njagi, E.C., Mei, M.C., and Suib, S.L. (2012). Gas-phase total

537   oxidation of benzene, toluene, ethylbenzene, and xylenes using shape-selective manganese

538   oxide and copper manganese oxide catalysts, *J. Phys. Chem. C*, **116**, 12066–12078.

539   Genuino, H.C., Meng, Y., Horvath, D.T., Kuo, C.H., Seraji, M.S., Morey, A.M., Joesten, R.L., and

540   Suib, S.L. (2013). Enhancement of catalytic activities of octahedral molecular sieve

541   manganese oxide for total and preferential CO oxidation through vanadium ion framework

542   substitution, *ChemCatChem*, **5**, 2306–2317.

543   Gomes, W.C.M., Neto, A. de O.W., Pimentel, P.M., Melo, D.M. de A., and Silva, F.R.G. e. (2013).

544   An in situ X-ray absorption spectroscopy study of copper nanoparticles in microemulsion,

545   *Colloids Surf. Physicochem. Eng. Asp.*, **426**, 18–25.

546   Hernandez, W.Y., Centeno, M.A., Ivanova, S., Eloy, P., Gaigneaux, E.M., and Odriozola, J.A.

547   (2012). Cu-modified cryptomelane oxide as active catalyst for CO oxidation reactions,

548   *Appl. Catal. B Environ.*, **123–124**, 27–35.

549   Hernandez, W.Y., Centeno, M.A., Romero-Sarria, F., Ivanova, S., Montes, M., and Odriozola,

550   J.A. (2010). Modified cryptomelane-type manganese dioxide nanomaterials for

551   preferential oxidation of CO in the presence of hydrogen, *Catal. Today*, **157**, 160–165.

552   Hou, J., Li, Y., Liu, L., Ren, L., and Zhao, X. (2013a). Effect of giant oxygen vacancy defects on

553   the catalytic oxidation of OMS-2 nanorods, *J. Mater. Chem. A*, **1**, 6736–6741.

554   Hou, J., Li, Y., Mao, M., Zhao, X., and Yue, Y. (2014). The effect of Ce ion substituted OMS-2

555   nanostructure in catalytic activity for benzene oxidation, *Nanoscale*, **6**, 15048–15058.

556   Hou, J., Liu, L., Li, Y., Mao, M., Lv, H., and Zhao, X. (2013b). Tuning the K^+ concentration in

557   the tunnel of OMS-2 nanorods leads to a significant enhancement of the catalytic activity

558   for benzene oxidation, *Environ. Sci. Technol.*, **47**, 13730–13736.

559 Hou, J., Sha, Z., Hartley, W., Tan, W., Wang, M., Xiong, J., Li, Y., Ke, Y., Long, Y., and Xue, S.

560   (2018). Enhanced oxidation of arsenite to arsenate using tunable K^+ concentration in the

561   OMS-2 tunnel, *Environ. Pollut.*, **238**, 524–531.

562 Iyer, A., Galindo, H., Sithambaram, S., King'ondu, C., Chen, C.H., and Suib, S.L. (2010).

563   Nanoscale manganese oxide octahedral molecular sieves (OMS-2) as efficient

564   photocatalysts in 2-propanol oxidation, *Appl. Catal. Gen.*, **375**, 295–302.

565 Jia, J., Zhang, P., and Chen, L. (2016). The effect of morphology of α-MnO_2 on catalytic

566   decomposition of gaseous ozone, *Catal. Sci. Technol.*, **6**, 5841–5847.

567 Jothiramalingam, R., Viswanathan, B., and Varadarajan, T.K. (2006a). Synthesis, characterization

568   and catalytic oxidation activity of zirconium doped K-OMS-2 type manganese oxide

569   materials, *J. Mol. Catal. Chem.*, **252**, 49–55.

570 Jothiramalingam, R., Viswanathan, B., and Varadarajan, T.K. (2006b). Synthesis and structural

571   characterization of copper incorporated manganese oxide OMS-2 materials synthesized via

572   potassium birnessite, *Mater. Chem. Phys.*, **100**, 257–261.

573 Kaewbuddee, C., Chanlek, N., and Wantala, K., (2019a). Effect of synthesized conditions of Cu-

574   K-OMS-2 on toluene oxidation performance, *Appl. Environ. Res.*, **41**, 83–95.

575 Kaewbuddee, C., Kidkhunthod, P., Chanlek, N., Khunphonoi, R., and Wantala, K. (2019b).

576   Chemical surface analysis on post-thermal treatment of the K-OMS-2 catalysts and

577   catalytic oxidation efficiency at low temperature, *Sains Malays.*, **48**, 1447–1457.

578 Kataoka, T., Yamazaki, Y., Singh, V.R., Fujimori, A., Chang, F.H., Lin, H.J., Huang, D., Chen,

579   C., Xing, G., Seo, J., Panagopoulos, C., and Wu, T. (2011). Ferromagnetic interaction

580   between Cu ions in the bulk region of Cu-doped ZnO nanowires, *Phys. Rev. B*, **84**, 153203.

581   Kim, M.S., Yang, J.B., Medvedeva, J., Yelon, W.B., Parris, P.E., and James, W.J. (2008).

582   Electronic structure of $La_{0.7}Sr_{0.3}Mn_{1-x}Cu_xO_3$ ($0.0 \le x \le 0.30$), *J. Phys. Condens. Matter*, **20**,

583   255228.

584   King'ondu, C., Opembe, N., Chen, C.H., Ngala, K., Huang, H., Iyer, A., Garces, H., and Suib, S.,

585   2011. Manganese oxide octahedral molecular sieves (OMS-2) multiple framework

586   substitutions: A new route to OMS-2 particle size and morphology control, *Adv. Funct.*

587   *Mater.*, **21**, 312–323.

588   Kumar, R., Sithambaram, S., and Suib, S.L., 2009. Cyclohexane oxidation catalyzed by manganese

589   oxide octahedral molecular sieves—Effect of acidity of the catalyst, *J. Catal.*, **262**, 304–

590   313.

591   Li, K., and Xue, D. (2006). Estimation of electronegativity values of elements in different valence

592   states, *J. Phys. Chem. A*, **110**, 11332–11337.

593   Li, Y., Fan, Z., Shi, J., Liu, Z., Zhou, J., and Shangguan, W. (2015). Modified manganese oxide

594   octahedral molecular sieves M′-OMS-2 (M′=Co,Ce,Cu) as catalysts in post plasma-

595   catalysis for acetaldehyde degradation, *Catal. Today*, **256**, 178–185.

596   Liu, H., Wang, A., Sun, Q., Wang, T., and Zeng, H. (2017). Cu nanoparticles/fluorine-doped tin

597   oxide (FTO) nanocomposites for photocatalytic H_2 evolution under visible light Irradiation,

598   *Catalysts*, **7**, 385.

599   Liu, J., Makwana, V., Cai, J., Suib, S.L., and Aindow, M. (2003). Effects of alkali metal and

600   ammonium cation templates on nanofibrous cryptomelane-type manganese oxide

601   octahedral molecular sieves (OMS-2), *J. Phys. Chem. B*, **107**, 9185–9194.

602 Liu, L., Song, Y., Fu, Z., Ye, Q., Cheng, S., Kang, T., and Dai, H. (2017). Effect of preparation

603 method on the surface characteristics and activity of the Pd/OMS-2 catalysts for the

604 oxidation of carbon monoxide, toluene, and ethyl acetate, *Appl. Surf. Sci.*, **396**, 599–608.

605 Liu, X.S., Jin, Z.N., Lu, J.Q., Wang, X.X., and Luo, M.F. (2010). Highly active CuO/OMS-2

606 catalysts for low-temperature CO oxidation, *Chem. Eng. J.*, **162**, 151–157.

607 Luo, J., Zhang, Q., Garcia-Martinez, J., and Suib, S.L. (2008). Adsorptive and acidic properties,

608 reversible lattice oxygen evolution, and catalytic mechanism of cryptomelane-type

609 manganese oxides as oxidation catalysts, *J. Am. Chem. Soc.*, **130**, 3198–3207.

610 Luo, J., Zhang, Q., Huang, A., and Suib, S.L. (2000). Total oxidation of volatile organic

611 compounds with hydrophobic cryptomelane-type octahedral molecular sieves,

612 *Microporous Mesoporous Mater.*, **35–36**, 209–217.

613 Ma, J., Wang, C., and He, H. (2017). Transition metal doped cryptomelane-type manganese oxide

614 catalysts for ozone decomposition, *Appl. Catal. B Environ.*, **201**, 503–510.

615 McManus, I.J., Daly, H., Manyar, H.G., Taylor, S.F.R., Thompson, J.M., and Hardacre, C. (2016).

616 Selective hydrogenation of halogenated arenes using porous manganese oxide (OMS-2)

617 and platinum supported OMS-2 catalysts, *Faraday Discuss.*, **188**, 451–466.

618 Morales-Torres, S., Perez-Cadenas, A.F., Kapteijn, F., Carrasco-Marin, F., Maldonado-Hodar,

619 F.J., Moulijn, J.A. (2009). Palladium and platinum catalysts supported on carbon nanofiber

620 coated monoliths for low-temperature combustion of BTX., *Appl. Catal. B Environ.*, **89**,

621 411–419.

622 Munoz-Rojas, D., Subias, G., Oro-Sole, J., Fraxedas, J., Martinez, B., Casas-Cabanas, M.,

623 Canales-Vazquez, J., Gonzalez-Calbet, J., Garcia-Gonzalez, E., Walton, R., and Casan-

624   Pastor, N. (2007). Ag$_2$CuMnO$_4$: A new silver copper oxide with delafossite structure, *J.*

625   *Solid State Chem*., **179**, 3883–3892.

626   Natarajan, K., Saraf, M., and Shaikh, M. (2018). Visible light driven water splitting through an

627   innovative Cu-treated-δ-MnO2 nanostructure: Probing enhanced activity and mechanistic

628   insights, *Nanoscale*, **10**, 13250–13260.

629   Ordonez, S., Bello, L., Sastre, H., Rosal, R., and Diez, F.V. (2002). Kinetics of the deep oxidation

630   of benzene, toluene, n-hexane and their binary mixtures over a platinum on γ-alumina

631   catalyst, *Appl. Catal. B Environ*., **38**, 139–149.

632   Ozacar, M., Poyraz, A.S., Genuino, H.C., Kuo, C.H., Meng, Y., and Suib, S.L. (2013). Influence

633   of silver on the catalytic properties of the cryptomelane and Ag-hollandite types manganese

634   oxides OMS-2 in the low-temperature CO oxidation, *Appl. Catal. Gen*., **462–463**, 64–74.

635   Pan, F., Liu, W., Yu, Y., Yin, X., Wang, Q., Zheng, Z., Wu, M., Zhao, D., Zhang, Q., Lei, X., and

636   Xia, D. (2016). The effects of manganese oxide octahedral molecular sieve chitosan

637   microspheres on sludge bacterial community structures during sewage biological

638   treatment, *Sci. Rep*., **6**, 37518.

639   Pan, R., Li, Y., Fang, F., and Cao, W. (2016). Surface valence states of Mn ions and magnetic

640   properties of La$_{0.67}$Sr$_{0.33}$MnO$_3$ Films, *Int. J. Mater. Sci. Eng*., **5**, 222–227.

641   Ramstad, A.L., and Mikkelsen, O. (2004). Structural characterisation of copper-containing

642   manganese oxide octahedral molecular sieve (Cu-OMS-2) materials by X-ray absorption

643   spectroscopy and cyclic voltammetry, *J. Mol. Struct*., **697**, 109–117.

644   Rebhan, B., Tollabimazraehno, S., Hesser, G., and Dragoi, V. (2015). Analytical methods used for

645   low temperature Cu–Cu wafer bonding process evaluation, *Microsyst. Technol*., **21**, 1003–

646   1013.

647 Roozeboom, F., Cordingley, P.D., and Gellings, P.J. (1981). Vanadium oxide monolayer catalysts:

648   The vapor-phase oxidation of methanol, *J. Catal.*, **68**, 464–472.

649 Said, S., Riad, M., Helmy, M., Mikhail, S., and Khalil, L. (2016). Preparation of nano-structured

650   cryptomelane materials for catalytic oxidation reactions, *J. Nanostructure Chem.*, **6**, 171–

651   182.

652 Santos, V.P., Bastos, S.S.T., Pereira, M.F.R., Orfao, J.J.M., and Figueiredo, J.L. (2010). Stability

653   of a cryptomelane catalyst in the oxidation of toluene, *Catal. Today*, **154**, 308–311.

654 Santos, V.P., Pereira, M.F.R., Orfao, J.J.M., and Figueiredo, J.L. (2011). Mixture effects during

655   the oxidation of toluene, ethyl acetate and ethanol over a cryptomelane catalyst, *J. Hazard.*

656   *Mater.*, **185**, 1236–1240

657 Santos, V.P., Pereira, M.F.R., Orfao, J.J.M., and Figueiredo, J.L. (2009). Catalytic oxidation of

658   ethyl acetate over a cesium modified cryptomelane catalyst, *Appl. Catal. B Environ.*, **88**,

659   550–556.

660 Santos, V.P., Soares, O.S.G.P., Bakker, J.J.W., Pereira, M.F.R., Orfao, J.J.M., Gascon, J.,

661   Kapteijn, F., Figueiredo, J.L. (2012). Structural and chemical disorder of cryptomelane

662   promoted by alkali doping: Influence on catalytic properties, *J. Catal.*, **293**, 165–174.

663 Schurz, F., Bauchert, J.M., Merker, T., Schleid, T., Hasse, H., and Glaser, R. (2009). Octahedral

664   molecular sieves of the type K-OMS-2 with different particle sizes and morphologies:

665   Impact on the catalytic properties in the aerobic partial oxidation of benzyl alcohol, *Appl.*

666   *Catal. Gen.*, **355**, 42–49.

667 Shaikjee, A., and Coville, N.J. (2011). The effect of copper catalyst reducibility on low

668   temperature carbon fiber synthesis, *Mater. Chem. Phys.*, **125**, 899–907.

669 Sharma, R.K., Gaur, R., Yadav, M., Goswami, A., Zboril, R., and Gawande, M.B. (2018). An

670 efficient copper-based magnetic nanocatalyst for the fixation of carbon dioxide at

671 atmospheric pressure, *Sci. Rep.*, **8**, 1–12.

672 Shen, X., Morey, A.M., Liu, J., Ding, Y., Cai, J., Durand, J., Wang, Q., Wen, W., Hines, W.A.,

673 Hanson, J.C., Bai, J., Frenkel, A.I., Reiff, W., Aindow, M., and Suib, S.L. (2011).

674 Characterization of the Fe-doped mixed-valent tunnel structure manganese oxide K-OMS-

675 2, *J. Phys. Chem. C*, **115**, 21610–21619.

676 Sihaib, Z., Puleo, F., Garcia-Vargas, J.M., Retailleau, L., Descorme, C., Liotta, L.F., Valverde,

677 J.L., Gil, S., and Giroir-Fendler, A. (2017). Manganese oxide-based catalysts for toluene

678 oxidation, *Appl. Catal. B Environ.*, **209**, 689–700.

679 Sinha, W., Sommer, M., Deibel, N., Ehret, F., Bauer, M., Sarkar, B., and Kar, S. (2015).

680 Experimental and theoretical investigations of the existence of CuII, CuIII, and CuIV in

681 copper corrolato complexes, *Angew. Chem. Int. Ed.*, **54**, 13769–13774.

682 Sithambaram, S., Xu, L., Chen, C.H., Ding, Y., Kumar, R., Calvert, C., and Suib, S.L. (2009).

683 Manganese octahedral molecular sieve catalysts for selective styrene oxide ring opening,

684 *Catal. Today*, **140**, 162–168.

685 Stelmachowski, P., Legutko, P., Jakubek, T., and Kotarba, A. (2018). Phase evolution and

686 electronic properties of cryptomelane nanorods, *J. Alloys Compd.*, **767**, 592–599.

687 Suib, S.L. (2008). Structure, porosity, and redox in porous manganese oxide octahedral layer and

688 molecular sieve materials, *J. Mater. Chem.*, 18, 1623–1631.

689 Sun, H., Chen, S., Wang, P., and Quan, X. (2011). Catalytic oxidation of toluene over manganese

690 oxide octahedral molecular sieves (OMS-2) synthesized by different methods, *Chem. Eng.*

691 *J.*, **178**, 191–196.

692   Sun, H., Liu, Z., Chen, S., and Quan, X. (2015). The role of lattice oxygen on the activity and

693   selectivity of the OMS-2 catalyst for the total oxidation of toluene, *Chem. Eng. J.*, **270**, 58–

694   65.

695   Sun, L., Cao, Q., Hu, B., Li, J., Hao, J., Jing, G., and Tang, X. (2011). Synthesis, characterization

696   and catalytic activities of vanadium–cryptomelane manganese oxides in low-temperature

697   NO reduction with NH_3, *Appl. Catal. Gen.*, **393**, 323–330.

698   Sun, M., Yu, L., Ye, F., Diao, G., Yu, Q., Hao, Z., Zheng, Y., and Yuan, L. (2013). Transition

699   metal doped cryptomelane-type manganese oxide for low-temperature catalytic

700   combustion of dimethyl ether, *Chem. Eng. J.*, **220**, 320–327.

701   Sun, M., Zhang, B., Liu, H., He, B., Ye, F., Yu, L., Sun, C., and Wen, H. (2017). The effect of

702   acid/alkali treatment on the catalytic combustion activity of manganese oxide octahedral

703   molecular sieves, *RSC Adv.*, **7**, 3958–3965.

704   Tarjomannejad, A., Farzi, A., Niaei, A., and Salari, D. (2016). An experimental and kinetic study

705   of toluene oxidation over $LaMn_{1-x}B_xO_3$ and $La_{0.8}A_{0.2}Mn_{0.3}B_{0.7}O_3$ (A=Sr, Ce and B=Cu, Fe)

706   nano-perovskite catalysts, *Korean J. Chem. Eng.*, **33**, 2628–2637.

707   Tomson, N.C., Williams, K.D., Dai, X., Sproules, S., DeBeer, S., Warren, T.H., and Wieghardt,

708   K. (2015). Re-evaluating the Cu K pre-edge XAS transition in complexes with covalent

709   metal–ligand interactions, *Chem. Sci.*, **6**, 2474–2487.

710   Tsai, Y.W., Tseng, Y.L., Sarma, L.S., Liu, D.G., Lee, J.F., and Hwang, B.J. (2004). Genesis of Pt

711   clusters in reverse micelles investigated by in situ X-ray absorption spectroscopy, *J. Phys.*

712   *Chem. B*, **108**, 8148–8152.

713 Wang, C., Ma, J., Liu, F., He, H., and Zhang, R. (2015). The effects of Mn^{2+} precursors on the

714 structure and ozone decomposition activity of cryptomelane-type manganese oxide (OMS-

715 2) catalysts, *J. Phys. Chem. C*, **119**, 23119–23126.

716 Wang, R., and Li, J. (2010). Effects of precursor and sulfation on OMS-2 catalyst for oxidation of

717 ethanol and acetaldehyde at low temperatures, *Environ. Sci. Technol.*, **44**, 4282–4287.

718 Wu, M.H., Shi, J., and Deng, H.P. (2018). Metal doped manganese oxide octahedral molecular

719 sieve catalysts for degradation of diclofenac in the presence of peroxymonosulfate, *Arab.

720 J. Chem.*, **11**, 924–934.

721 Wu, Y., Feng, R., Song, C., Xing, S., Gao, Y., and Ma, Z. (2017). Effect of reducing agent on the

722 structure and activity of manganese oxide octahedral molecular sieve (OMS-2) in catalytic

723 combustion of o-xylene, *Catal. Today*, **281**, 500–506.

724 Wu, Y., Liu, M., Ma, Z., and Xing, S. tao. (2011). Effect of alkali metal promoters on natural

725 manganese ore catalysts for the complete catalytic oxidation of o-xylene, *Catal. Today*,

726 **175**, 196–201.

727 Yang, Y., Huang, J., Zhang, S., Wang, S., Deng, S., Wang, B., and Yu, G. (2014). Catalytic

728 removal of gaseous HCBz on Cu doped OMS: Effect of Cu location on catalytic

729 performance, *Appl. Catal. B Environ.*, **150–151**, 167–178.

730 Yodsa-nga, A., Millanar, J.M., Neramittagapong, A., Khemthong, P., and Wantala, K. (2015).

731 Effect of manganese oxidative species in as-synthesized K-OMS 2 on the oxidation of

732 benzene, *Surf. Coat. Technol.*, **271**, 217–224.

733 Yun, L., Li, Y., Zhou, C., Lan, L., Zeng, M., Mao, M., Liu, H., and Zhao, X. (2017). The formation

734 of CuO/OMS-2 nanocomposite leads to a significant improvement in catalytic performance

735 for NO reduction by CO, *Appl. Catal. A-Gen.*, **530**, 1–11.

Figure captions

Figure 1. XRD pattern of copper-doped K-OMS-2 samples compared with undoped K-OMS-2 catalyst.

Figure 2. The XANES feature of (a) the Mn K-edge spectra and (b) Cu K-edge spectra of Cu-K-OMS-2 catalyst compared with the copper standards and manganese standards, respectively.

Figure 3. The XPS results of (a) Cu 2p, (b) Mn 2p and (c) O 1s spectra of the Cu-K-OMS-2 materials.

Figure 4. EXAFS analysis (a) Mn K-edge, (b) Cu K-edge of prepared Cu-K-OMS-2 catalyst These spectra were obtained by measurements and the cryptomelane Q structure model fitting as represented by the black and red lines, respectively.

Figure 5. The Cu-K-OMS-2 structure.

Figure 6. The catalytic activity of K-OMS-2 and Cu-K-OMS-2 catalysts.

Figure 7. (a) The initial reaction rate of toluene oxidation versus reaction temperature and (b) the natural log of initial reaction rate of toluene oxidation versus inverse reaction temperature.
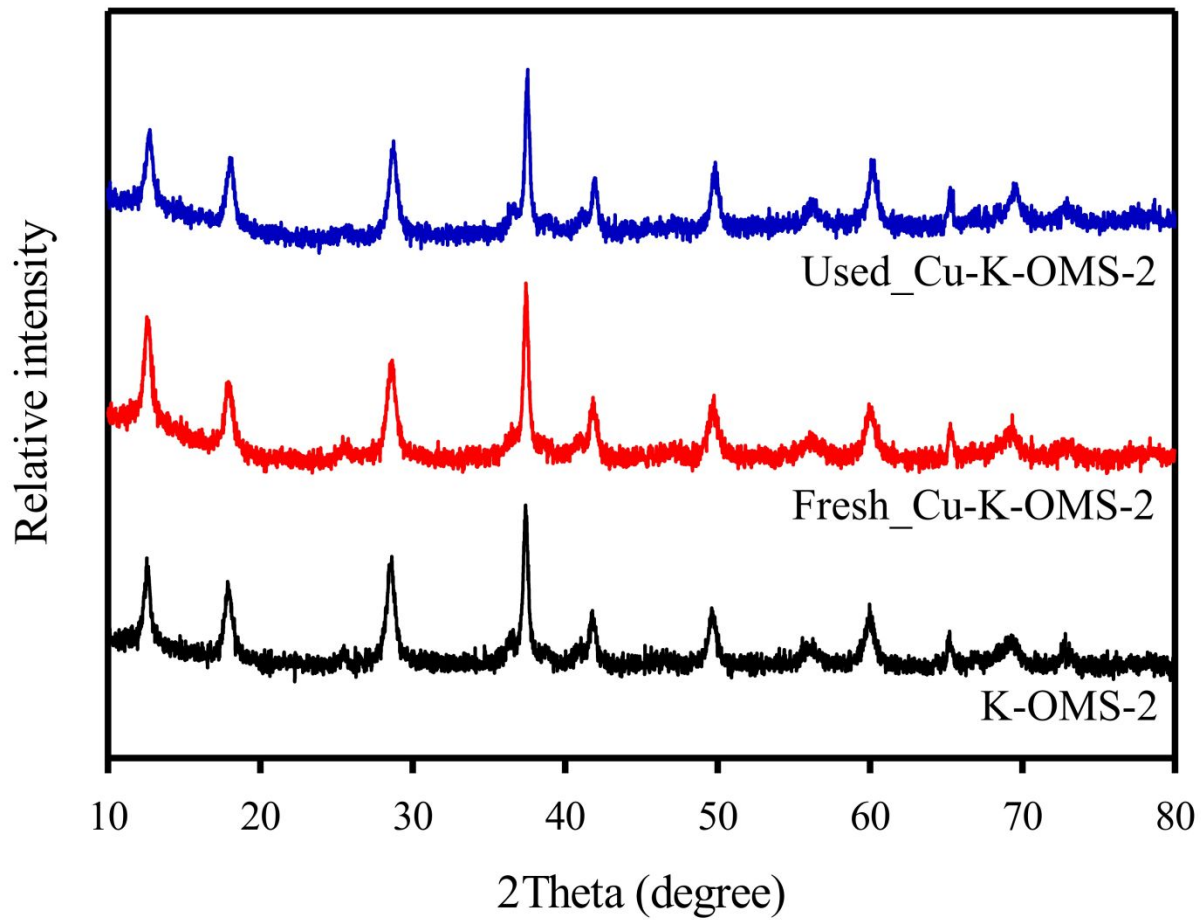
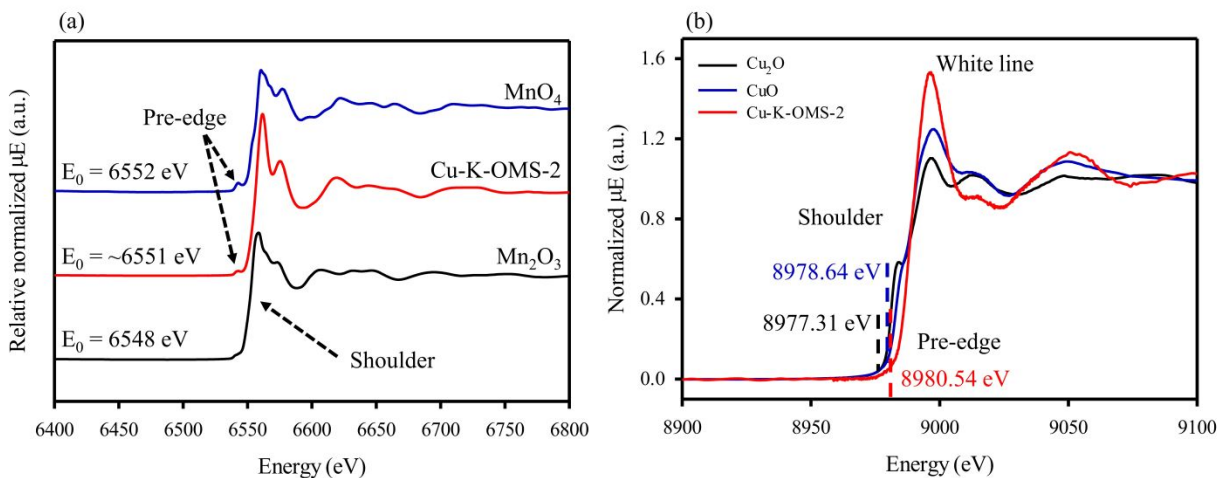Figure 1. XRD pattern of copper-doped K-OMS-2 samples compared with undoped K-OMS-2 catalyst.
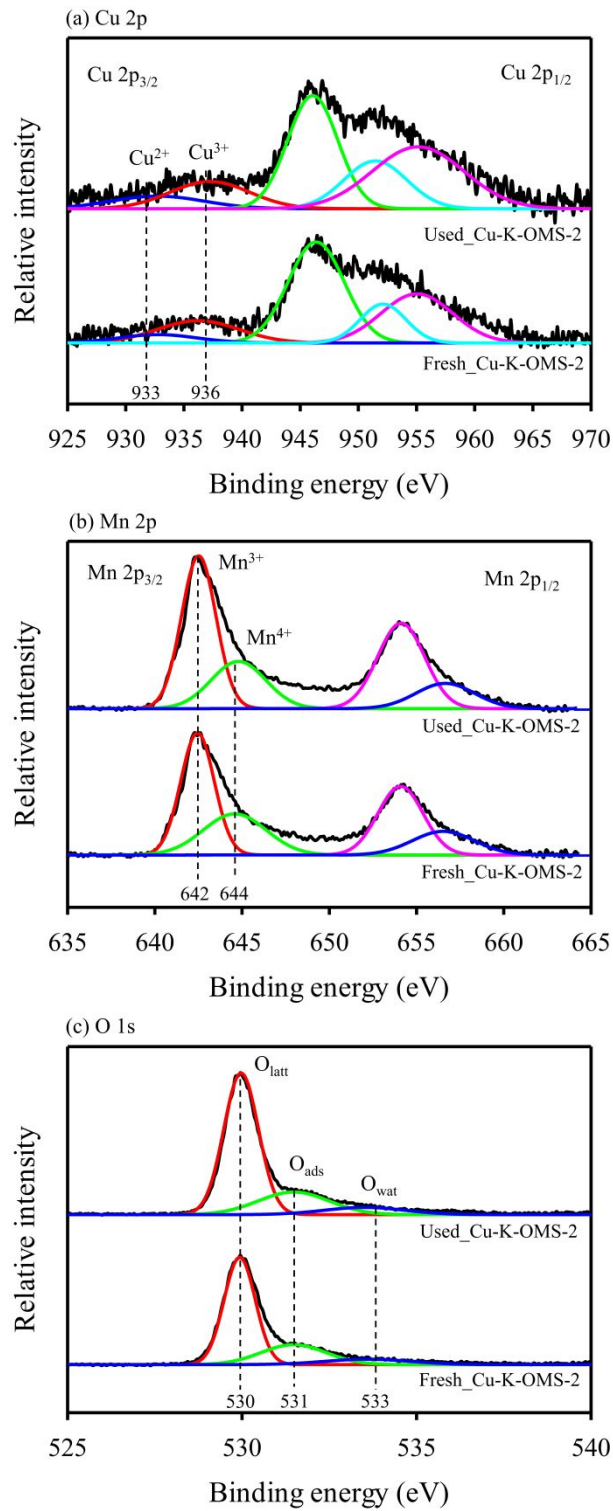
Figure 2. The XANES feature of (a) the Mn K-edge spectra and (b) Cu K-edge spectra of Cu-K-OMS-2 catalyst compared with the copper standards and manganese standards, respectively.

Figure 3. The XPS results of (a) Cu 2p, (b) Mn 2p and (c) O 1s spectra of the Cu-K-OMS-2 materials.
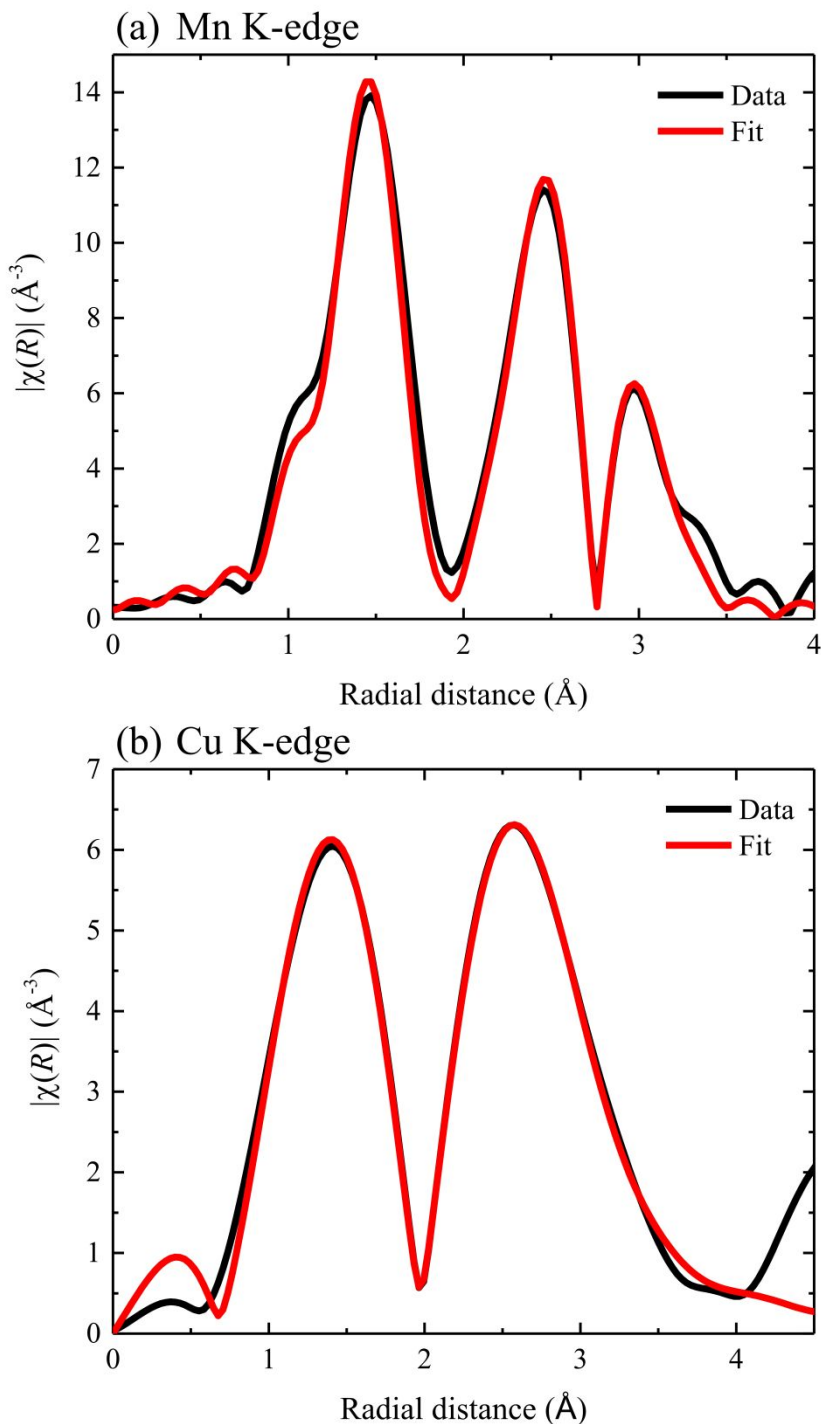
Figure 4. EXAFS analysis (a) Mn K-edge, (b) Cu K-edge of prepared Cu-K-OMS-2 catalyst

These spectra were obtained by measurements and the cryptomelane Q structure model fitting as

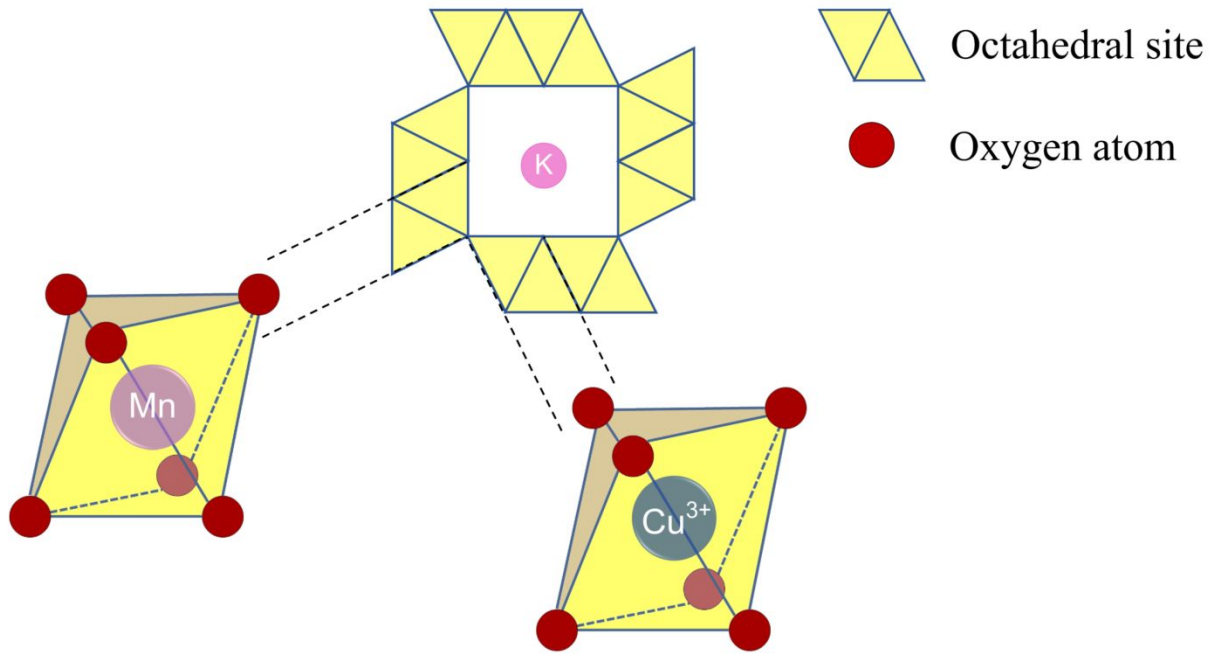represented by the black and red lines, respectively.
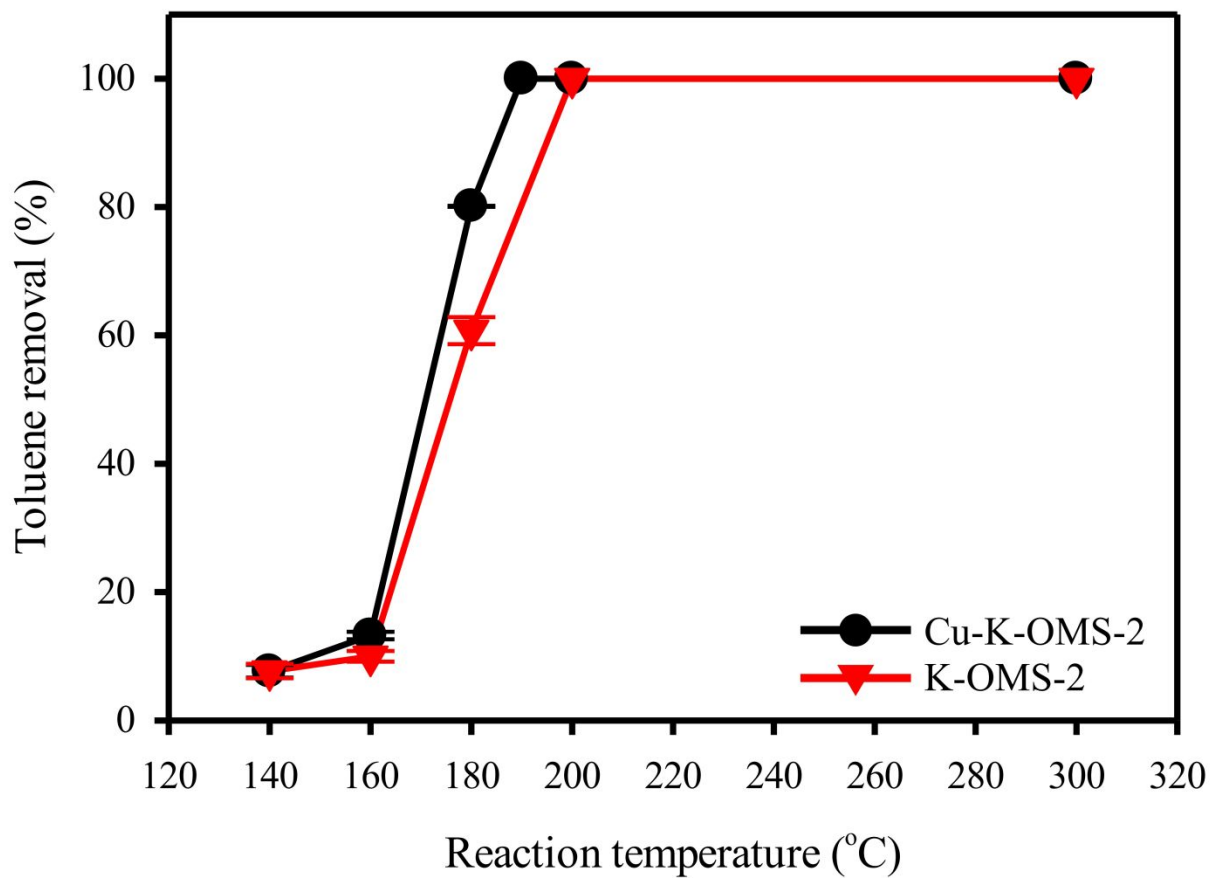
Figure 5. The Cu-K-OMS-2 structure.

Figure 6. The catalytic activity of K-OMS-2 and Cu-K-OMS-2 catalysts.

Figure 7. (a) The initial reaction rate of toluene oxidation versus reaction temperature and (b) the

natural log of initial reaction rate of toluene oxidation versus inverse reaction temperature.

Table captions

Table 1. The physicochemical properties of Cu-K-OMS-2 materials compared with undoped K-OMS-2 material.

Table 2. EXAFS fitting results of Mn and Cu atoms as a central atom in the MnO_6 site.

Table 3. The comparisons of the activation energy and the catalytic performance on toluene removal.

Table 1. The physicochemical properties of Cu-K-OMS-2 materials compared with undoped K-OMS-2 material.

Catalysts	Specific surface area (m^2/g)	Mn^{3+}/Mn^{4+} ratio[a]	Cu^{3+}/Cu^{2+} ratio[b]	O$_{ads}$/O$_{latt}$ Ratio[b]
K-OMS-2	51.31	0.10	-	0.24
Cu-K-OMS-2	60.74	0.08	2.83	0.62

[a]The Mn^{3+}/Mn^{4+} ratio was calculated by using the LCF of XANES spectra.

[b]The Cu^{3+}/Cu^{2+} ratio and O$_{ads}$/O$_{latt}$ ratio were calculated by using the XPS data.

1
2
3
4
5
6
7
8
9
10
11
12
13
14
15
16
17
18
19
20
21
22
23
24
25
26
27
28
29
30
31
32
33
34
35
36
37
38
39
40
41
42
43
44
45
46
47
48
49
50
51
52
53
54
55
56
57
58
59
60

Table 2. EXAFS fitting results of Mn and Cu atoms as a central atom in the MnO_6 site.

	MnO$_6$ site with Mn atom				MnO$_6$ site with Cu atom		
Correlations	Coor. no.	Distance (Å)	σ^2 (Å^2)	Correlations	Coor. no.	Distance (Å)	σ^2 (Å^2)
Mn–O1	6	1.888 ± 0.005	0.004 ± 0.001	Cu–O1	6	1.920 ± 0.014	0.008 ± 0.001
Mn–Mn1	4	2.869 ± 0.007	0.005 ± 0.001	Cu–Cu1	4	2.767 ± 0.027	0.013 ± 0.004
Mn–O2	3	3.212 ± 0.021	0.004 ± 0.003	Cu–O2	3	3.756 ± 0.032	0.001 ± 0.001
Mn–Mn2	4	3.430 ± 0.001	0.005 ± 0.001	Cu–Cu2	4	3.290 ± 0.021	0.001 ± 0.001
Mn–O3	3	3.242 ± 0.021	0.004 ± 0.003	Cu–O3	3	3.785 ± 0.032	0.001 ± 0.001

Table 3. The comparisons of the activation energy and the catalytic performance on toluene removal.

Catalysts	E_a (kJ mol^{-1})	Inlet concentration (ppmV)	Reaction temperature (°C)	References
Pt/γ-Al$_2$O$_3$	106	5000	$T_{50} \sim 180$	Ordonez et al., 2002
Pt/ACNF	128	1000	$T_{95} \sim 190$	Morales-Torres et al., 2009
Pt/γ-Al$_2$O$_3$	138	1000	$T_{85} \sim 190$	Morales-Torres et al., 2009
Pd/ACNF	161	1000	$T_{50} \sim 190$	Morales-Torres et al., 2009
Pd/γ-Al$_2$O$_3$	116	1000	$T_{25} \sim 190$	Morales-Torres et al., 2009
Cu-K-OMS-2	91	7,550	$T_{100} = 190$	This work